Available online at www.sciencedirect.com
ScienceDirect
Trans. Nonferrous Met. Soc. China 32(2022) 4156−4170
Transactions of Nonferrous Metals Society of China
www.tnmsc.cn

Preparation of magnetic core−shell Ce-doped zirconia and its As(III) adsorption properties

Ming-han DU[1], Hong YANG[1], Weng FU[2], Yan-ling HU[1], Huan TAO[1], Jia-xi FAN[3], Ying LIU[1], Yu-fan CHEN[1], Na-er DILI[1], Xiao-qing LIU[1]

1. Jiangsu Key Laboratory of Resources and Environmental Information Engineering, China University of Mining and Technology, Xuzhou 221116, China;
2. School of Chemical Engineering, The University of Queensland, St Lucia, Queensland 4072, Australia;
3. Nanjing Zhuoze Water Conservancy Technology Co., Ltd., Nanjing 210000, China

Received 29 September 2021; accepted 15 August 2022

Abstract: A new magnetic mesoporous As(III) adsorbent of Fe_3O_4@SiO_2@Ce-ZrO_2 was prepared by solvothermal and sol−gel method. The core−shell adsorbent presented a high specific surface area (168.2 m^2/g) and fast magnetic separation performance (5.37 A·m^2/kg). Compared with Fe_3O_4@SiO_2@ZrO_2, the Ce-doped sample exhibited 12%−23% increase in As(III) uptake over pH 3−11, which was mainly attributed to the formation of bimetal M—O—As complexes. The coexisted SO_4^{2-} and PO_4^{3-} weakened As(III) adsorption, Ca^{2+} worked oppositely, but the impact of Cl^- and NO_3^- was negligible. The As(III) maximum adsorption capacity was 24.52 mg/g at 313 K with an initial As(III) concentration of 5 mg/L at pH 7, and its kinetics was well fitted by the pseudo-second-order model. Moreover, the adsorbent exhibited remarkable recyclability. It is suggested that Fe_3O_4@SiO_2@Ce−ZrO_2 is a promising adsorbent for the advanced treatment of As(III) contaminated wastewater.

Key words: core−shell structure; magnetism; cerium doping; zirconia; As(III) adsorption

1 Introduction

As(III) is 60 times more toxic than As(V) [1] and is ranked as a kind of Class 1 carcinogen reported by the World Health Organization [2]. When As(III) and its compounds are ingested, they can be accumulated in the human body, mainly hair, nails, bones, livers and kidneys [3]. As(III) in water bodies mainly comes from anthropogenic (e.g., metallurgy and mining, arsenic-containing pesticides, industrial wastewater) and natural sources (e.g., natural sediments) [4]. It was reported that the wastewater from the abandoned Onyeama Coal Mine contained 9.9−39.6 mg/L of As(III) [5]. Therefore, As(III) removal should be priority [6]. Common methods for heavy metal pollution control include coagulation and precipitation [7], electrochemistry [8], reverse osmosis [9], membrane separation [10], ion exchange [11], oxidation [12] and adsorption [13]. For instance, the lime powder is often used for arsenic precipitation. But its deficiency might not be overlooked, such as large amounts of hazardous precipitate wastes and undesirable As(III) residual concentration in the treated liquor [14].

Adsorbents with high specific surface areas can adsorb arsenic species through physical and chemical processes. The adsorption technology has great potential especially in low concentrations of As(III) removal [15] due to good treatment effect, simple device and convenient maintenance. However, traditional adsorbents are subject to limitations such as low adsorption capacity, a little

Corresponding author: Hong YANG, Tel: +86-516-83591320, E-mail: yanghong_cumt@163.com
DOI: 10.1016/S1003-6326(22)66085-0

bit high loss rate and long contact time [16]. Thus, synthesis of multifunctional adsorbents has been a hot scientific issue for the arsenic removal.

The core−shell nanosphere is a typical representative of such novel adsorbents. Magnetic cores such as Fe_3O_4 are used for magnetic separation to the alleviate adsorbent loss. As an ideal coating for the magnetic core, silicon dioxide (SiO_2) can effectively prevent the magnetic particles from agglomeration thus to enhance their dispersion stabilities. Meanwhile, it is considered as the intermediate sphere with plenty of hydroxyl groups (—OH) to bind outer sites. Fe_3O_4@SiO_2 was reported to be synthesized and loaded with hydrated lanthanum oxide layer for the phosphorous removal [17].

Metal oxides are certificated with stable As(III) adsorption performance. The chitosan coated Fe_3O_4@$Zr(OH)_4$ was hydrothermally prepared [18]. It maintained 76.02% of the initial arsenite adsorption capacity even after 5 cycles. Furthermore, the doping of rare earth elements helps to improve arsenic removal of iron, titanium, aluminum and other oxides [19−21]. La-doped alumina had twice higher adsorption capacity than that of purely activated alumina based on the As−O−La bonding [20]. The arsenic uptake of Ce−Ti composite oxides was better than that of single TiO_2 and CeO_2 counterparts [21].

To achieve a high adsorption rate, mesoporous structures with the pore diameter ranging from 2 to 50 nm have been introduced into the adsorbent preparation. Compared with the non-mesoporous sample, mesoporous Mg−Al LDH unfolded faster mass transfer and greater phthalate removal [22]. Rarely does the magnetic core−shell material have double mesoporous spheres [23]. In addition, mesoporous SiO_2 sphere was testified to be more stable in the alkaline environment. It was found that the non-porous SiO_2 was easily etched by 0.6 mol/L Na_2CO_3, while mesoporous SiO_2 layer was well preserved due to the more stable Si—O network [24].

In this work, a newly multifunctional adsorbent of Ce-doped core−shell zirconia with a magnetic core and double mesoporous spheres was prepared based on solvothermal method followed by two steps of sol−gel coating. The physic-chemical and structural traits of Fe_3O_4@SiO_2@Ce-ZrO_2 were characterized. The effects of initial pH values and coexistent ions on As(III) removal were subsequently investigated. The isothermal and kinetic adsorption properties of As(III) were discussed to explore the uptake mechanism. Moreover, its regeneration ability was evaluated.

2 Experimental

2.1 Materials and methods

2.1.1 Synthesis of Fe_3O_4

Fe_3O_4 powders were prepared by solvothermal method using polyvinyl pyrrolidone (PVP, AR), ferric chloride ($FeCl_3·6H_2O$, AR), sodium acetate (NaAc, AR) and ethylene glycol (EG, AR). In a typical run, 3 g PVP, 4.5 g $FeCl_3·6H_2O$ and 6 g NaAc were mixed into 90 mL EG with 2 h stirring to form a kind of yellow viscous liquid. The mixture was poured into a stainless steel reactor lined with poly tetra fluoroethylene (PTFE) and heated at 200 °C for 8 h. When the reactor was cooled, the resulting solid was magnetically separated, and washed with ethanol and deionized water. Finally, it was dried under vacuum at 60 °C for 1 d to obtain Fe_3O_4 powder.

2.1.2 Synthesis of Fe_3O_4@SiO_2 and Fe_3O_4@SiO_2@Ce-ZrO_2

Ce-doped core−shell zirconia was prepared based on two-step sol−gel method using the synthesized Fe_3O_4 powders, PVP, tetraethyl orthosilicate (TEOS, AR), absolute ethanol (EtOH, AR), tetramethylammonium hydroxide (TMAOH, 25 wt.%), zirconium butoxide (ZB, 80 wt.%) and cerium nitrate ($Ce(NO_3)_3·6H_2O$, AR).

In the first step of sol−gel coating, 1 g PVP was ultrasonically mixed in 20 mL deionized water for 10 min. Then, 0.1 g Fe_3O_4 particles were added and well dispersed for another 30 min. After that, 100 mL EtOH, 10 mL deionized water and 2 mL TMAOH were added and mixed for 10 min. Meanwhile, 3 mL TEOS was dissolved in 20 mL EtOH for 10 min. The diluted TEOS was subsequently dropped into the above mixture. The new formed turbid liquid was ultrasonically stirred for 30 min and mechanically stirred for 3 h at room temperature. After reaction, the product of Fe_3O_4@SiO_2 was magnetically separated, and washed with ethanol and deionized water.

In the second step of sol−gel coating, the Fe_3O_4@SiO_2 microparticles were flushed into a conical flask with 100 mL EtOH and 10 mL

deionized water, and scattered by ultrasound for 30 min. With the addition of TMAOH (2 mL), the mixture was ultrasonically reacted with another 10 min. Meanwhile, 2 mL ZB and a series of $Ce(NO_3)_3·6H_2O$ (Ce:Zr = 0%, 1%, 2%, 3%, 4%, 5% and 6%, in at.%) were also ultrasonically diluted in 20 mL EtOH for 10 min. Then the latter solution was dropwise added into the former under ultrasonic shaking for 30 min. The final turbid liquid was mechanically stirred for 3 h at room temperature. Afterwards, the product of Fe_3O_4@SiO_2@Ce-ZrO_2 was magnetically separated, washed with ethanol and deionized water, and dried under vacuum at 60 °C for 1 d.

2.2 Characterization

The morphology of the core−shell material was characterized by the transmission electron microscope (TEM, Tecnai G2F20). Nitrogen adsorption−desorption analysis was performed at 77 K (Micromeritics ASAP 2460) to determine the pore structural parameters. Element contents were collected with the energy dispersive spectroscopy (EDS, Quanta FEG 250). The zeta potentials of adsorbents were determined using the zeta potential analyzer (ZPA, Otsuka ELSZ−2000). The magnetization curves of synthesized particles were recorded by the vibrating sample magnetometer (VSM, Quanta PPMS−9). The As(III) valences were revealed using the X-ray photoelectron spectroscopy (XPS, Escalab 250Xi). The Fourier transform infrared spectra were obtained using KBr pellets (FTIR, Bruker Vertex 80V).

2.3 As(III) adsorption tests

2.3.1 Influence of Ce doping amount

To compare As(III) adsorption capacities onto the undoped and Ce-doped samples, 10 mg Fe_3O_4@SiO_2@ZrO_2 and a sequence of Fe_3O_4@SiO_2@Ce-ZrO_2 were separately mixed with 50 mL As(III) ($NaAsO_2$, AR) solution under pH 7 and stirred at 200 r/min for 1 h. The resulting mixture was magnetically separated, then the supernate was filtered through the 0.45 μm membrane to avoid the disturbance of As(III) detection from possible particles, and the filtrate was analyzed via the arseno-antimono-molybdenum blue spectrophotometry. As expressed in Eq. (1), the As(III) loading capacities with different doping samples were then calculated by the change in concentration between the filtrate and the initial As(III) solution (5 mg/L).

$$Q_t=(C_0-C_t)\cdot V/m \tag{1}$$

where Q_t is the adsorption capacity at time t (mg/g), V is the volume of aqueous solution (L), m is the adsorbent dosage (g), C_0 is the initial As(III) concentration (mg/L), and C_t is the As(III) concentration at time t (mg/L).

2.3.2 Influence of initial pH

The nitric acid (HNO_3) and NaOH were used to adjust the initial pH values. In a typical run, 10 mg Fe_3O_4@SiO_2@Ce-ZrO_2 (4 at.%) were mixed with 100 mL As(III) solution under stirring at 200 r/min for 1 h.

2.3.3 Influence of coexisting ions

A procedure similar to which described above was followed, except that different amounts of metal salts ($NaSO_4$, Na_3PO_4, NaCl, $NaNO_3$ and $CaCl_2$) were added respectively to form 0, 0.2, 2 and 5 mmol/L of coexistent ion solutions under neutral conditions.

2.4 Adsorption isotherm test

10 mg Fe_3O_4@SiO_2@Ce-ZrO_2 and 100 mL As(III) solution (0.5, 1.0, 2.0, 5.0 and 10 mg/L) were placed in conical bottles and then stirred at 293, 303 and 313 K for 1 h under neutral conditions.

2.5 Adsorption kinetics test

10 mg Fe_3O_4@SiO_2@Ce-ZrO_2 and 100 mL As(III) solution (1.0, 2.0 and 5.0 mg/L) were placed in conical bottles and stirred at 293 K for 5, 10, 15, 20, 30, 45, 60 and 90 min under neutral conditions.

2.6 Influence of adsorbent dosage on low-concentration As(III) adsorption

Different amounts of Fe_3O_4@SiO_2@Ce-ZrO_2 (5, 10, 15, 20, 25 and 30 mg) were mixed into 100 mL As(III) solution with the concentration of 0.8 mg/L, and stirred at 293 K for 1 h under neutral conditions.

2.7 Adsorbent regeneration test

The As-loaded sample was used to verify the regeneration capacity. In a typical run, 0.05 g Fe_3O_4@SiO_2@Ce-ZrO_2 and 100 mL As(III) solution (5.0 mg/L) were placed in the conical bottle and stirred for 1 h at room temperature under

neutral conditions. The resulting mixture was magnetically separated, then the supernate was filtered through the 0.45 μm membrane, and the filtrate was analyzed via the arseno-antimono-molybdenum blue spectrophotometry. Then, the As-loaded adsorbent was placed in 100 mL 0.1 mol/L NaOH, and stirred for 6 h to elute As(III) species at room temperature. After filtration, the adsorbent was washed and neutralized, and then was used again. Following another filtration, the regenerated sample was dried in a vacuum oven at 60 °C before another cycle.

3 Results and discussion

3.1 Effect of Ce doping amount on As(III) adsorption

The equilibrium As(III) adsorption capacities (Q_e) onto samples with different Ce doping amounts (0−6 at.%) are compared in Fig. 1. Q_e values increased first but then decreased with the rise of Ce doping amount. Moderate Ce doping undoubtedly improved more efficient As(III) removal, whereas too much Ce content was adverse to stably heterogenous Ce−ZrO_2 framework, hence crippled As(III) adsorption. The sample with 4 at.% Ce doping had the highest As(III) removal.

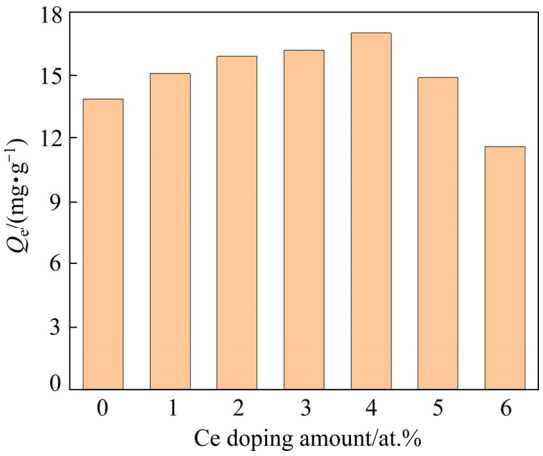

Fig. 1 Effect of Ce doping amount on As(III) adsorption

3.2 Characterization of Fe_3O_4@SiO_2@Ce-ZrO_2

Based on the preliminary tests, 4 at.% Ce doping was screened for the synthesis of Fe_3O_4@SiO_2@Ce-ZrO_2. The TEM image (Fig. 2(a)) presents an overall outline of the nanosphere with core−shell structure. Figure 2(b) displays the rough and uneven shell, thus provides ample contact sites for As(III) adsorption.

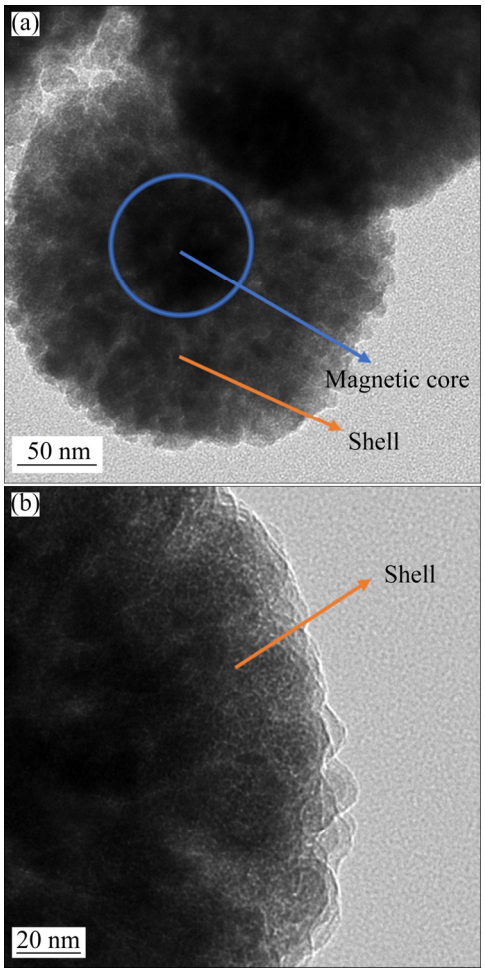

Fig. 2 TEM images of overall outline (a) and partial enlargement (b) of Fe_3O_4@SiO_2@Ce-ZrO_2

The mesoporous structures of prepared materials are verified by the N_2 adsorption−desorption data (Fig. 3 and Table 1). The isotherms reveal hysteresis loops, which conforms to the type-IV curve, at the relative pressure of 0.4−0.9. And the core−shell nanosphere has higher specific surface area (168.2 m^2/g) compared with the uncoated Fe_3O_4 core (38.23 m^2/g). Moreover, the formation of mesopores is also proved by BJH adsorption apertures within the scope of 2−50 nm. All the mesoscopic characteristics support easier access to the high As(III) adsorption capacity of Fe_3O_4@SiO_2@Ce-ZrO_2.

To ascertain the state of double shells and As(III) removal, the EDS results of Fe_3O_4@SiO_2@Ce-ZrO_2 before and after adsorption are performed in Fig. 4. The existence of Si, Ce and Zr implies the successful Ce doping and shell coatings (Fig. 4(a)), and meanwhile, the As(III) appearance (Fig. 4(b)) indicates the visible As(III) adsorption

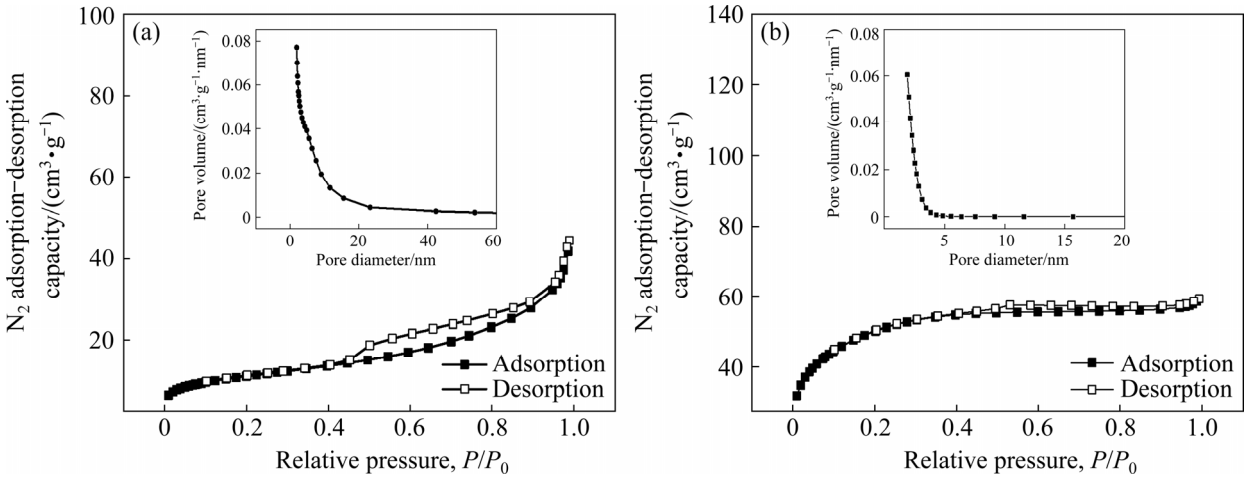

Fig. 3 Nitrogen adsorption−desorption isotherms and pore size distribution curves of Fe_3O_4 (a) and Fe_3O_4@SiO_2@Ce-ZrO_2 (b)

Table 1 Structural parameters of Fe_3O_4 and Fe_3O_4@SiO_2@Ce-ZrO_2

Material	Average pore diameter/nm	Pore volume/(cm³·g⁻¹)	Specific surface area/(m²·g⁻¹)
Fe_3O_4	7.972	0.05038	38.23
Fe_3O_4@SiO_2@Ce-ZrO_2	2.631	0.08788	168.2

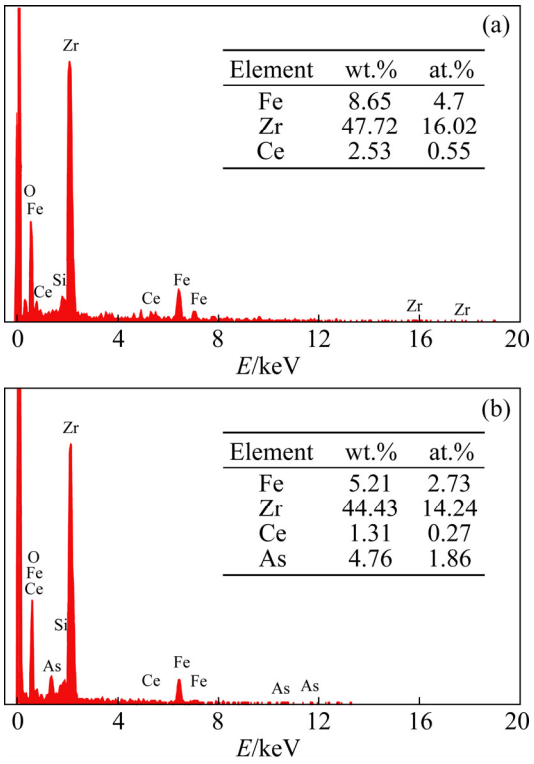

Fig. 4 EDS results of Fe_3O_4@SiO_2@Ce-ZrO_2 before (a) and after (b) As(III) adsorption

onto the prepared core−shell nanosphere. In addition, the determined 3.43 at.% qualitatively reflected active compositions of the nanomaterial. And more precise Ce/Zr molar ratio of 4.09 at.% was tested via ICP method, which conformed to the corresponding synthetic ratio.

Magnetic properties of synthetic samples are recorded by VSM (Fig. 5). With the increase of coating shells, the saturated magnetization significantly decreased from 39.80 A·m²/kg (naked Fe_3O_4) to 27.66 A·m²/kg (Fe_3O_4@SiO_2, one coating shell), finally to 5.37 A·m²/kg (Fe_3O_4@SiO_2@Ce-ZrO_2, two coating shells). Optical photos (Fig. 6) are well in accord with the VSM results. Burrs caused by the magnetic separation gradually decayed

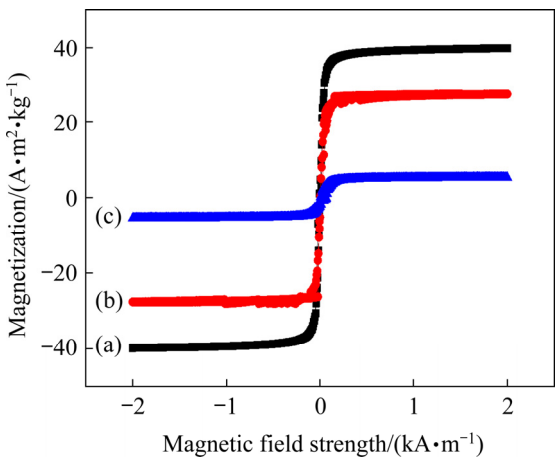

Fig. 5 Magnetization curves of Fe_3O_4 (a), Fe_3O_4@SiO_2 (b) and Fe_3O_4@SiO_2@Ce-ZrO_2 (c)

with the shell coating. Nevertheless, the sample of Fe_3O_4@SiO_2@Ce-ZrO_2 emerged the good performance of magnetic separation.

3.3 Effect of initial pH on As(III) adsorption

The initial pH has significant effects on the arsenite species, as well as on surface properties of the adsorbent. As shown in Fig. 7(a), As(III) adsorption of samples with and without Ce doping are comparatively evaluated in the pH range of 3−11. The As(III) adsorbed amount firstly rose with the pH increase from 3 to 5, kept stably at the second stage (pH 5−9), and then decreased in the relatively strong alkaline condition (pH 9−11). Such status could be resulted from As(III) existence forms and the surface potential of nanospheres at different pH values. Nonionic H_3AsO_3, as the dominant As(III) species, exists when pH < 9.2 [25]. Further pH increase resulted in the rise of anionic $H_2AsO_3^-$ and $HAsO_3^{2-}$. In turn, the zeta potential changes of two adsorbents versus pH are depicted in Fig. 7(b). Both points of zero charge (PZC) emerged at pH 6−7, so the highest As(III) uptake was produced mainly from the formation of surface complexes between non-charged H_3AsO_3 and the nanospheres. No repulsive forces but positively charged outer shell easily retarded As(III) transfer at $pH < pH_{PZC}$, which was reported to be unfavorable for As(III) adsorption [26]. On the contrary, As(III) adsorption was depressed especially when pH > 9.2 because the deprotonation of hydroxyl groups gradually strengthened the electrostatic repulsion between arsenite and adsorbent [27].

Despite the same trend of As(III) adsorption, Fe_3O_4@SiO_2@Ce-ZrO_2 exhibited 12%−23% greater As(III) uptake capacity than Fe_3O_4@SiO_2@ZrO_2. They achieved the utmost As(III) equilibrium adsorption amount of 17.43 mg/g and 14.39 mg/g at pH 7, respectively. Figure 7(b)

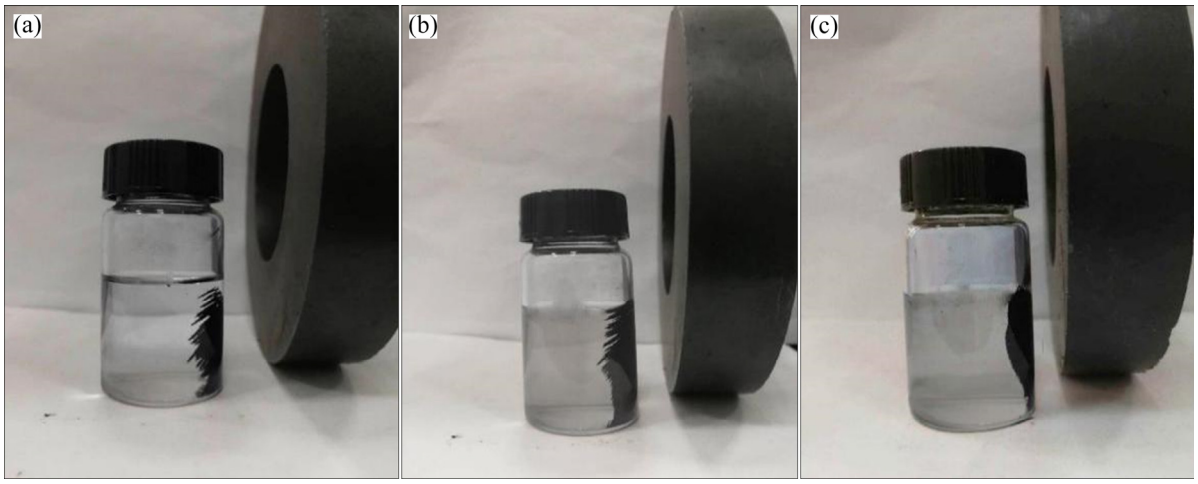

Fig. 6 Magnetic separation comparison among Fe_3O_4 (a), Fe_3O_4@SiO_2 (b) and Fe_3O_4@SiO_2@Ce-ZrO_2 (c)

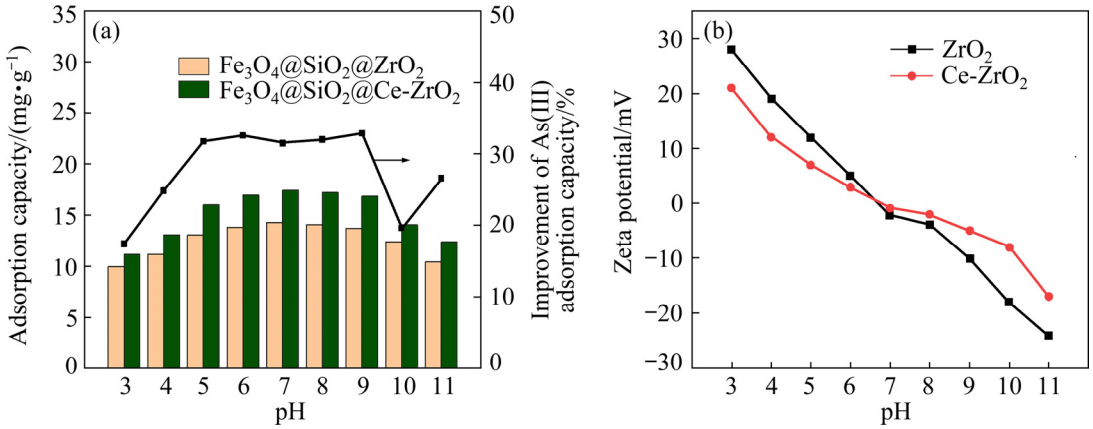

Fig. 7 Effect of initial pH on As(III) adsorption by Fe_3O_4@SiO_2@ZrO_2 and Fe_3O_4@SiO_2@Ce-ZrO_2 (a), and zeta potential curves of two adsorbents (b)

reveals that the electrostatic force is weakened by Ce doping, and the Ce-doped sample is favorable for the arsenic complex promotion due to the appreciable As(III) affinity of CeO_2 without oxidation [28]. In this work, the As(III) removal performance of Fe_3O_4@SiO_2@Ce-ZrO_2 was determined at pH 7, which was suitable for actual water and wastewater treatment [29].

3.4 Effect of coexistent ions on As(III) adsorption

Five common coexistent ions of SO_4^{2-}, PO_4^{3-}, Cl^-, NO_3^- and Ca^{2+} with different concentrations were selected to investigate the competitive effect on As(III) adsorption. As shown in Fig. 8, the existence of Cl^- and NO_3^- has little negative influence on As(III) uptake, while the presence of Ca^{2+} displays a positive effect to some extent. The As(III) adsorbed amount increased by 8.1% when the initial Ca^{2+} concentration was up to 5 mmol/L. Calcium oxides are generally used as co-precipitators for As(III) removal. The Ca^{2+} ions are deemed to stick around the adsorbent surface and strengthen its positive charges, which is beneficial to the negative arsenite adsorption. At the same time, Ca^{2+} ions helped to form multiple Ce−As−Ca−As and Zr−As−Ca−As complexes. Thus, As(III) adsorption could be facilitated by electrostatic attraction and surface complex formation [30]. It is recommended to use the adsorption process as advanced As(III) removal especially after the lime precipitation. The As(III) removal was noticeably interfered with SO_4^{2-}, since the sulfate (up to 480 mg/L) competitively occupied the surface active sites of adsorbents [31].

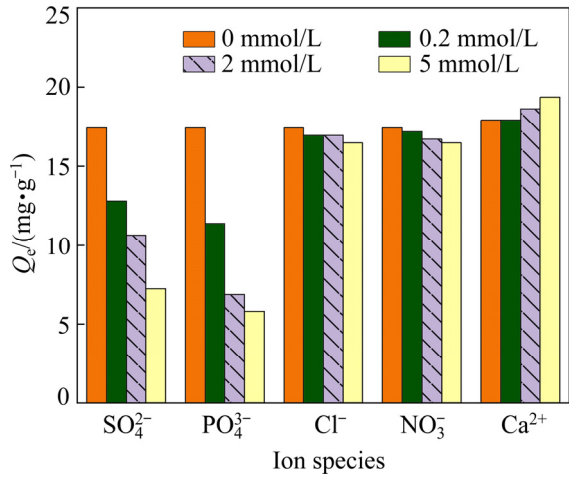

Fig. 8 Effect of coexistent ion species and concentrations on As(III) adsorption by Fe_3O_4@SiO_2@Ce-ZrO_2

The greatest drop of As(III) adsorption was resulted from the attendance of PO_4^{3-}, which had the similar structure to arsenic anion species and contended for binding sites on the Ce-doped zirconia shell. These results are consistent with previous reports about arsenic adsorption on different types of adsorbents [32].

3.5 As(III) adsorption isotherms of Fe_3O_4@SiO_2@Ce-ZrO_2

Adsorption is usually set up after conventional processes such as precipitation and coagulation to ensure residual arsenic concentration to meet requisite discharge or utilization standards. Thus, the arsenic removal ability of adsorbents is more significant and practical at the low concentration. The batch experiment of As(III) adsorption onto Fe_3O_4@SiO_2@Ce-ZrO_2 was conducted in the initial concentration range of 0.5−10 mg/L at 293, 303 and 313 K under neutral conditions. Three common isotherm models of Langmuir, Freundlich and Temkin were used to fit the As(III) adsorption data of the prepared adsorbent.

The Langmuir model, given as Eq. (2), assumes that the adsorption takes place at specific homogeneous sites within the adsorbent and the maximum adsorption corresponds to a saturated monolayer of adsorbate matrixes on the adsorbent surface [33].

$$Q_e=\frac{Q_m K_L C_e}{1+K_L C_e} \tag{2}$$

In addition, a dimensionless constant separation factor (R_L) is used to determine the favorability of the adsorption process. R_L values expressed as Eq. (3), indicate the type of Langmuir isotherm to be irreversible (R_L=0), favorable (0<R_L<1), linear (R_L=1) or unfavorable (R_L>1) [33].

$$R_L=\frac{1}{1+K_L C_0} \tag{3}$$

where Q_e is the equilibrium loading capacity of adsorbent (mg/g), C_e and C_0 are the equilibrium and initial concentrations of the adsorbate (mg/L), Q_m is the maximum adsorption capacity corresponding to complete monolayer coverage (mg/g), and K_L is the Langmuir adsorption equilibrium constant (L/mg).

As an empirical isotherm, the Freundlich model is often used for nonideal and multilayer

adsorption that involves heterogeneous surface energy systems. It is defined as Eq. (4) [34].

$$Q_e = K_F C_e^{1/n} \quad (4)$$

where K_F is the Freundlich adsorption coefficient ($mg^{1+1/n} \cdot g^{-1} \cdot L^{-1/n}$), and n is the Freundlich constant.

Generally, the adsorption capacity of an adsorbent for a given adsorbate augments with the increase of K_F, and the n value implies the adsorption intensity and favorable adsorption (n>1).

The Temkin model describes an energy relationship in which the adsorption heat decreases linearly with the adsorbed amount. It belongs to the heterogeneous multilayer adsorption, and the adsorption energy of active sites is uniformly distributed. It is defined as [35]

$$Q_e = A \ln(B_T C_e) \quad (5)$$

where C_e is the remaining adsorbate concentration in adsorption equilibrium (mg/L), and A and $\ln B_T$ are two constants.

The measured As(III) adsorption data were fitted to three isotherms at three different temperatures in Fig. 9. The fitting parameters and correlation coefficients of isotherms are listed in Tables 2 and 3.

As shown in Fig. 9 and Table 2, R^2 values of three isotherm models increase as the following order: Temkin < Freundlich < Langmuir. The best fit of Langmuir model demonstrates that the mechanism of As(III) removal is mainly attributed to monolayer adsorption. On the other hand, high R^2 values (>0.85) of Freundlich and Temkin models cannot be ignored, so heterogeneous surface adsorptions coexist with homogeneous counterparts.

All values of R_L and n in Tables 2 and 3 indicate that the synthetic core−shell sample is a favorable As(III) adsorbent from effluents. Furthermore, in the range of test temperature (293−313 K), Q_e value was elevated with temperature rise, but it gradually slowed down and finally the adsorption tended to be saturated, which proved that such adsorption process was a spontaneously endothermic reaction. Meanwhile, the maximum As(III) adsorption capacity onto Fe_3O_4@SiO_2@Ce-ZrO_2 reached 24.52 mg/g (313 K). The synthesized Zr−Ce bimetal oxides on the outer sphere promotes the increase of surface hydroxyl species to form more arsenic complexes [36]. Its notable As(III) uptake performance at such low As(III) concentrations is comparable or even much higher than those reported adsorbents (Table 4).

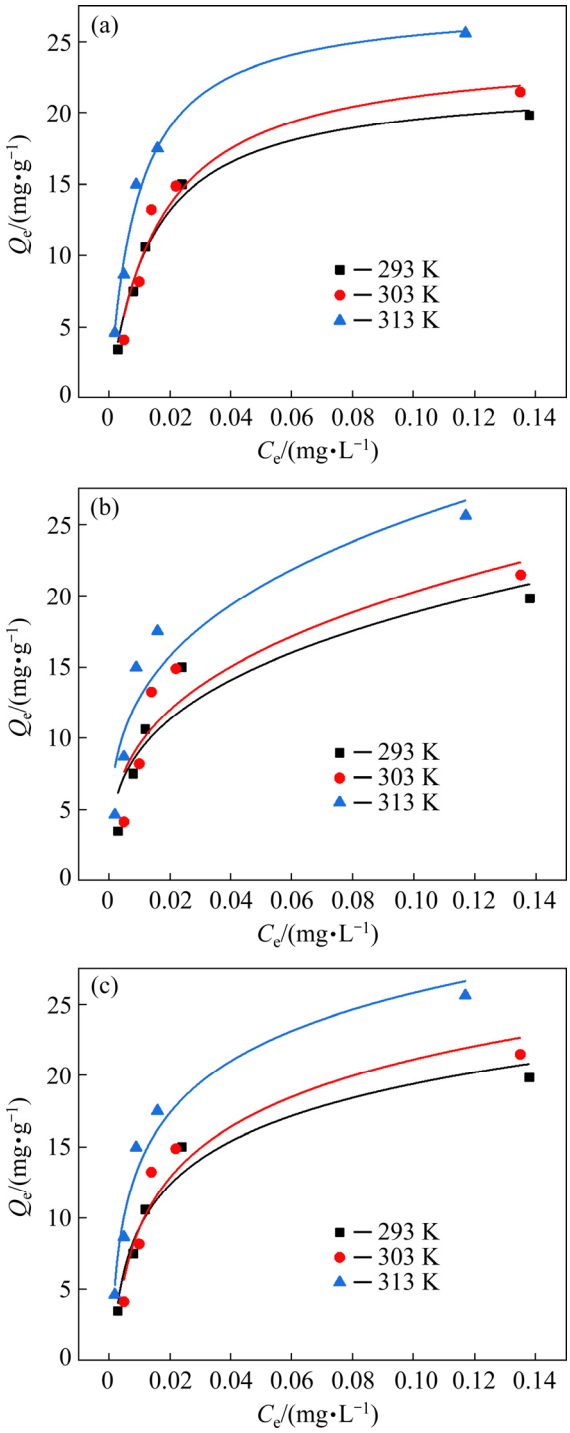

Fig. 9 Langmuir (a), Freundlich (b) and Temkin (c) isotherm fittings of As(III) adsorption onto Fe_3O_4@SiO_2@Ce-ZrO_2

Table 2 Langmuir, Freundlich and Temkin isotherm parameters and correlation coefficients of As(III) adsorption onto Fe_3O_4@SiO_2@Ce-ZrO_2 at 293, 303 and 313 K

Model	Isotherm parameter	293 K	303 K	313 K
Langmuir	R^2	0.9859	0.9775	0.9901
	Q_m/(mg·g^{-1})	17.96	19.81	24.52
	K_L/(L·mg^{-1})	0.8271	0.8488	0.6263
Freundlich	R^2	0.9775	0.9699	0.9851
	n	1.993	1.982	2.401
	K_F/(mg$^{1+1/n}$·g^{-1}·L$^{-1/n}$)	8.288	9.279	9.689
Temkin	R^2	0.8763	0.8637	0.9338
	A	4.986	5.398	6.797
	B_T	5.136	5.440	4.315

Table 3 R_L values of As(III) adsorption onto Fe_3O_4@SiO_2@Ce-ZrO_2 under different initial As(III) concentrations at 293, 303 and 313 K

Initial As(III) concentration/(mg·L^{-1})	R_L		
	293 K	303 K	313 K
0.5	0.7047	0.7020	0.7615
1	0.5473	0.5409	0.6149
2	0.3768	0.3707	0.4439
5	0.1947	0.1907	0.2420
10	0.1079	0.1054	0.1377

3.6 As(III) adsorption kinetics of Fe_3O_4@SiO_2@Ce-ZrO_2

Many adsorption applications need rapid adsorption rate and short contact time. The As(III) adsorption kinetic data were fitted by pseudo-first-order and pseudo-second-order models (Eqs. (6) and (7)) [45].

$$Q_t = Q_e[1-\exp(-k_1 t)] \tag{6}$$

$$Q_t = \frac{k_2 Q_e^2 t}{1+k_2 Q_e t} \tag{7}$$

where t is the contact time (min), k_1 is the rate constant of pseudo-first-order adsorption (min^{-1}), and k_2 is the rate constant of pseudo-second-order adsorption (g·mg^{-1}·min^{-1}).

The fitting profiles of As(III) adsorption kinetics under neutral conditions are shown in Fig. 10. The tendency of adsorption data indicates that the As(III) adsorbed amounts are enlarged with increasing equilibrium concentration, which is consistent with the adsorption isotherm situations (Fig. 9). It is noted that the As(III) adsorption of Fe_3O_4@SiO_2@Ce-ZrO_2 reached the equilibrium state more rapidly, and required less time than that of previously reported adsorbents [2]. The As(III) uptake ascended dramatically and about 96.88% of the equilibrium adsorption capacity was achieved within 30 min, then the adsorption equilibrium was set up within 1 h. It can be ascribed to the existence of affluent adsorption sites and the accessible mesostructure for ion transfer.

Results of experimental Q_e ($Q_{e,exp}$), calculated Q_e ($Q_{e,cal}$) and other kinetic parameters are summarized in Table 5. The pseudo-second-order model was fitted well based on the comparison of R^2 values, and $Q_{e,exp}$ data are much closer to the $Q_{e,cal}$ of the pseudo-second-order model [46]. This demonstrates that the rate-limiting step of As(III) removal is mainly controlled by chemisorption mechanism.

Table 4 As(III) adsorption comparison of various adsorbents at different As(III) concentrations

Adsorbent	Initial As(III) concentration/(mg·L^{-1})	Adsorption capacity/(mg·g^{-1})	pH	Source
Fe_3O_4@SiO_2@Ce-ZrO_2	5	24.52	7	This work
Modified saxaul tree ash	25	25.60	7	[37]
Aminated carbon nanotubes/polyaniline	4	19.10	6–8	[38]
TiO_2/chitosan/graphene oxide composite	50	10.98	7.2	[39]
Hydrous iron-nickel-manganese trimetal oxide	10	18.65	7.2	[40]
Biochar from bamboo waste modified with iron	50	22.32	7	[41]
Commercial nanomagnetite	40	6.68	7	[42]
Fe(III)−Si binary oxide	40	16.74	7.4	[43]
Zn−Al−SO_4 layered double hydroxide	10	13.20	7	[44]

3.7 Removal efficiency of low-concentration As(III) by Fe_3O_4@SiO_2@Ce-ZrO_2

Since As(III) adsorption is widely used as a kind of advanced wastewater treatment, accompanied by cost considerations, a balance needs to be found between the removal efficiency and the adsorbent dosage. Based on the adsorption kinetic results, different doses of Fe_3O_4@SiO_2@Ce-ZrO_2 were stirred with 0.8 mg/L of As(III) solution for 1 h to investigate the As(III) removal efficiencies at low concentrations. The C_e values in Fig. 11 decreased but removal efficiencies rose with the dosage increase. Over 99% of arsenite removal efficiency was observed with the dosage of 0.20 g/L. The sample of Fe_3O_4@SiO_2@Ce-ZrO_2 presents fine As(III) enrichment at the low concentrations.

3.8 As(III) adsorption mechanism of Fe_3O_4@SiO_2@Ce-ZrO_2

To further understand the mechanism of As(III) adsorption onto Fe_3O_4@SiO_2@Ce-ZrO_2, XPS results (Fig. 12) of the adsorbent were performed for the comparison of microcosmic changes before and after As(III) adsorption. The full-range XPS in Fig. 12(a) exhibited the involved elements of Fe, Si, Zr, Ce and O, and clear As 3d peak after adsorption was consistent with the EDS images (Fig. 4). Zr 3d and Ce 3d binding energies (Fig. 12(b)) were observed to slightly shift to higher zones, which indicated the coordination between As(III) and bimetal sites after adsorption [47]. O1s peaks located at 530−531 eV (Fig. 12(c)) were considered as hydroxyl groups on the outer sphere, and the —OH share decreased from 41.81% to 33.86% due to the As(III) replacement by ligand exchange and surface complexation. Simultaneously, a wide As 3d peak with binding energy of 44.5 eV (Fig. 12(d)) emerged and the increased proportion attributed to As(III)—O bonding. It is also proved that no oxidation reacted between As(III) and the adsorbent.

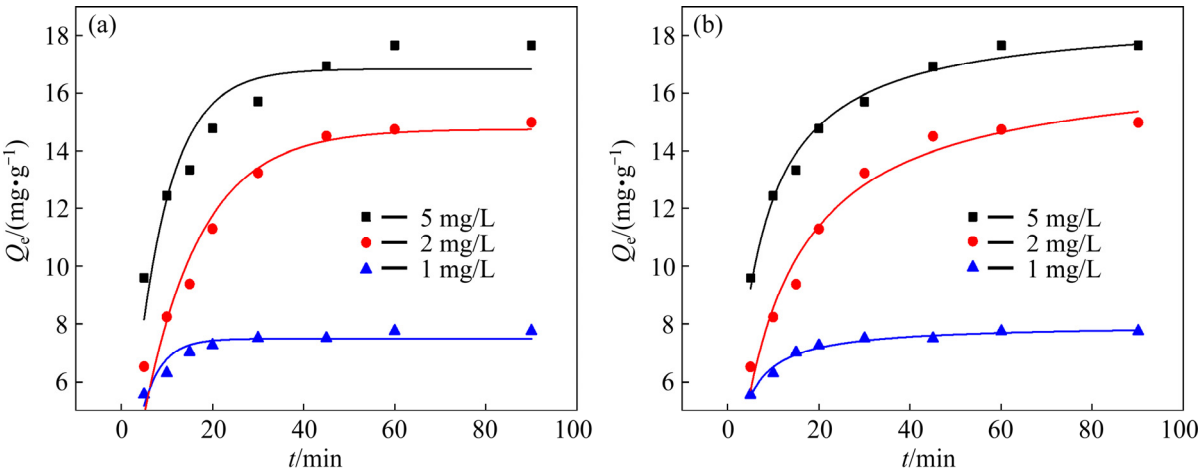

Fig. 10 Pseudo-first-order (a) and pseudo-second-order (b) kinetic fittings of As(III) adsorption onto Fe_3O_4@SiO_2@Ce-ZrO_2

Table 5 Pseudo-first-order and pseudo-second-order kinetic parameters for As(III) removal with Fe_3O_4@SiO_2@Ce-ZrO_2

Initial As(III) concentration/ (mg·L^{-1})	Experimental equilibrium adsorption amount	Pseudo-first-order kinetic model			Pseudo-second-order kinetic model		
	$Q_{e,exp}$/ (mg·g^{-1})	R^2	$Q_{e,cal}$/ (mg·g^{-1})	k_1/min^{-1}	R^2	$Q_{e,cal}$/ (mg·g^{-1})	k_2/ (g·mg^{-1}·min^{-1})
1	7.748	0.8317	7.486	0.5433	0.9758	7.987	0.05538
2	15.12	0.9384	14.77	0.1833	0.9664	17.1	0.00585
5	17.7	0.8714	16.85	0.3037	0.9841	18.73	0.01033

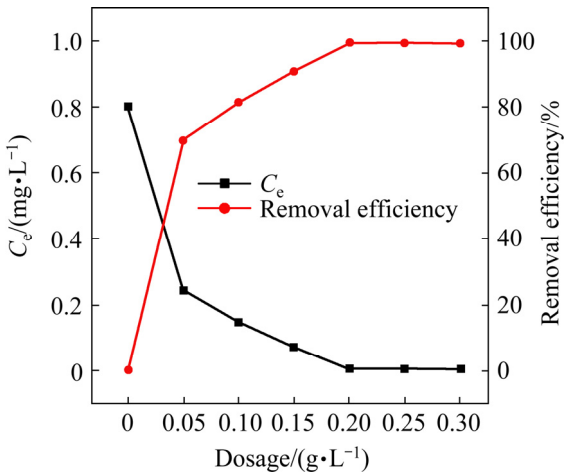

Fig. 11 Effect of adsorbent dosage on As(III) adsorption with initial concentration of 0.8 mg/L

In addition, FTIR spectra in the range of 4000−500 cm^{-1} in Fig. 13 give a proof for the formation of M—O—As complex (M=Zr and Ce). The peak at 3480 cm^{-1} corresponds to —OH stretching vibrations of water molecules [48]. The feature items around 959 and 797 cm^{-1} resulted from Si—O moieties were barely changed, which illustrated that the inter silica sphere did not involve the As(III) adsorption reaction. It is found that band intensities located at 1637, 1552, 1339, 1492 and 1215 cm^{-1}, corresponding to the Zr—OH and Ce—OH bending vibrations, were weakened after arsenite adsorption, thus to reveal the pivotal role of M—OH groups in the process of As(III) ligand exchange and complexation [49]. Moreover, a new peak at 884 cm^{-1} (As—O stretching mode) emerges in the As-loaded sample, and confirms As(III) adsorption onto the Ce-doped zirconia at the outer sphere.

Based on the XPS and FTIR analyses, the As(III) adsorption mechanism is presented in Fig. 14. Hydroxyl groups are formed on the outer shells of wet nanospheres. Meanwhile, arsenic

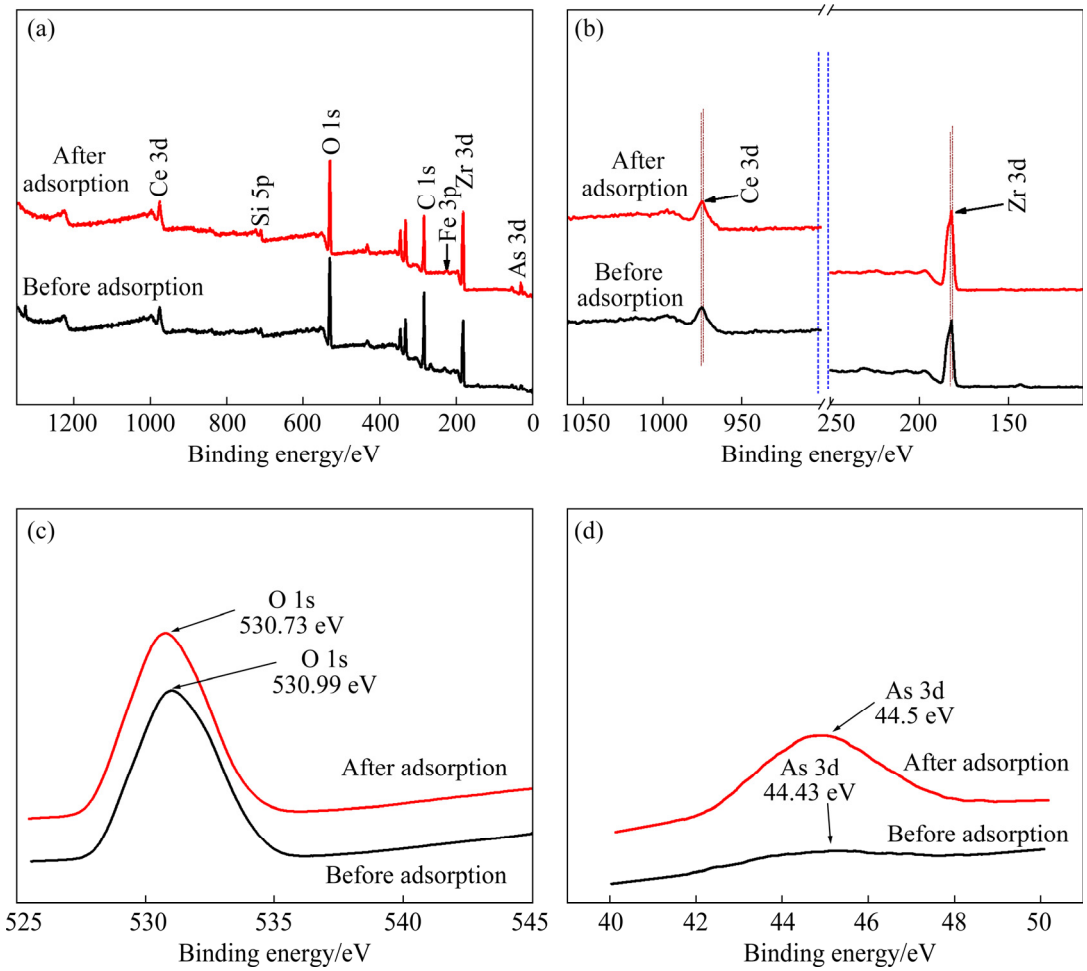

Fig. 12 XPS results of full-range (a), Zr 3d and Ce 3d (b), O 1s (c) and As 3d (d) of Fe_3O_4@SiO_2@Ce-ZrO_2 before and after As(III) adsorption

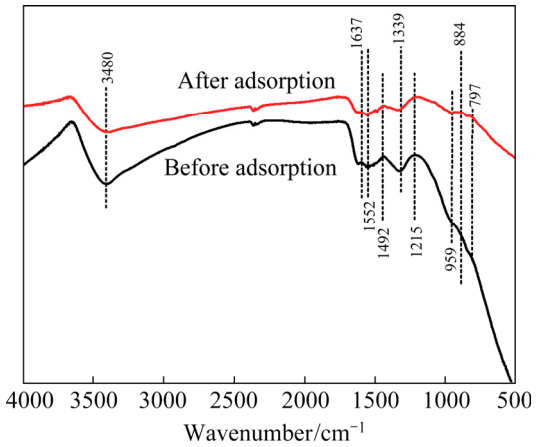

Fig. 13 FTIR spectra of Fe_3O_4@SiO_2@Ce-ZrO_2 before and after As(III) adsorption

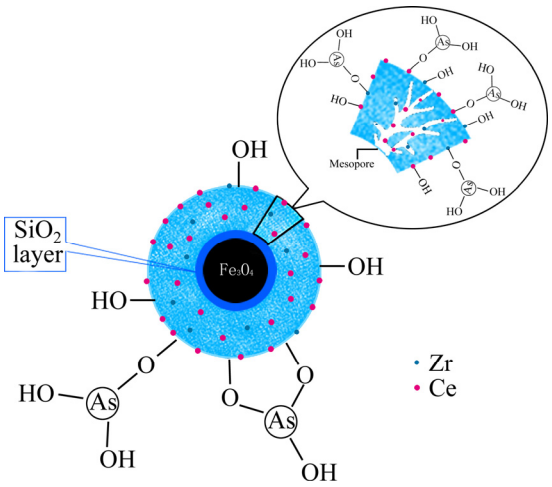

Fig. 14 Schematic diagram of As(III) adsorption mechanism by Fe_3O_4@SiO_2@Ce-ZrO_2

species rapidly diffuse into the mesopores and ligand exchanges are engendered with M—OH groups. And then, M—O—As complexation leads to As(III) removal.

3.9 Regeneration and reuse of Fe_3O_4@SiO_2@Ce-ZrO_2

To evaluate the regeneration performance of Fe_3O_4@SiO_2@Ce-ZrO_2, sequential adsorption−desorption tests were conducted over five cycles. According to the As(III) uptake mechanism of the above adsorbent, the adsorption−desorption operation depends on the pH change of the solution. It is reasonable that the As(III)-loaded sample could be recovered under basic condition [50]. The As(III) equilibrium adsorption amount (Q_e) and removal efficiency values in every cycle are shown in Fig. 15, and 0.1 mol/L NaOH was proved to be feasible as the As(III) strippant. The As(III) adsorption capacity onto Fe_3O_4@SiO_2@Ce-ZrO_2 could keep at a relatively high level (>92%) even after 5 cycles, which was beneficial from the significant structure properties such as the markedly magnetic separation due to Fe_3O_4 core and the stable protection of mesoporous SiO_2 inter sphere, well connected mesopores channels and plenty of active adsorption sites on the outer sphere. It is indicated that the obtained adsorbent has the potential for practical wastewater treatment.

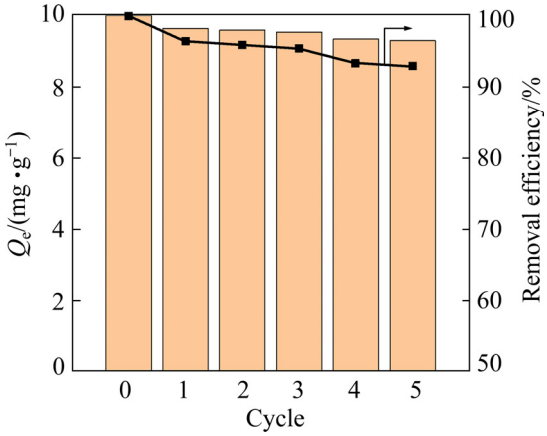

Fig. 15 Adsorption−desorption cycles of Fe_3O_4@SiO_2@Ce-ZrO_2

4 Conclusions

(1) A novel As(III) adsorbent (Fe_3O_4@SiO_2@Ce-ZrO_2) with the core−shell nanostructure was prepared via the combination of solvothermal and sol−gel methods. It exhibited saturated magnetization of 5.37 A·m^2/kg and mesoporous morphology with the specific surface area of 168.2 m^2/g.

(2) With the formation of bimetal M—O—As complexes on the outer sphere, Fe_3O_4@SiO_2@Ce-ZrO_2 achieved 12%−23% larger As(III) uptake than the counterpart of Fe_3O_4@SiO_2@ZrO_2 in the pH range of 3−11. Its maximum As(III) adsorption capacity reached 24.52 mg/g at 313 K with an initial As(III) concentration of 5 mg/L under pH 7. Coexisted Cl^- and NO_3^- (except SO_4^{2-} and PO_4^{3-}) ions had ignorable influence on the As(III) removal, while the presence of Ca^{2+} even gave the positive effect.

(3) The nanosphere of Fe_3O_4@SiO_2@Ce-ZrO_2 has great virtues including visibly magnetic separation, rapid mass transfer, amply functional

groups and stable regeneration ability. So, it is suitable for advanced purification of arsenic wastewater.

Acknowledgments

The authors acknowledge the financial support from the Open Research Fund of Jiangsu Key Laboratory of Resources and Environmental Information Engineering, China (No. JS201810).

References

[1] XU Hui, YAO Li-wei, XU Qiu-jing, WANG Yun-yan, MIN Xiao-bo, KE Yong, LUO Yong-jian, TANG Jin-yao, PENG Si-ang, ZHANG Li-min, DU Jia-li. Process and mechanism of hydrothermal stabilization for arsenic sulfide sludge containing elemental sulfur [J]. Transactions of Nonferrous Metals Society of China, 2022, 32(3): 1041−1049.

[2] LIU Deng-chao, DENG Shu-bo, MAIMAITI A, WANG Bin, HUANG Jun, WANG Yu-jue, YU Gang. As(III) and As(V) adsorption on nanocomposite of hydrated zirconium oxide coated carbon nanotubes [J]. Journal of Colloid and Interface Science, 2018, 511: 277−284.

[3] GUO Hua-ming, ZHANG Bo, LI Yuan, BERNER Z, TANG Xiao-hui, NORRA S, STUBEN D. Hydrogeological and biogeochemical constrains of arsenic mobilization in shallow aquifers from the Hetao Basin, Inner Mongolia [J]. Environmental Pollution, 2011, 159(4): 876−883.

[4] SMEDLEY P L, KINNIBURGH D G. A review of the source, behaviour and distribution of arsenic in natural waters [J]. Applied Geochemistry, 2002, 17(5): 517−568.

[5] OZOKO D C. Heavy metal geochemistry of acid mine drainage in Onyeama Coal Mine, Enugu, Southeastern Nigeria [J]. Journal of Environment and Earth Science, 2015, 5(10): 120−127.

[6] XU Yi-fan, LI Hao, ZENG Xian-chun. A novel biofilm bioreactor derived from a consortium of acidophilic arsenite-oxidizing bacteria for the cleaning up of arsenite from acid mine drainage [J]. Ecotoxicology, 2021, 30(7): 1437−1445.

[7] HUO Qiang, LIU Xi, CHEN Li-jun, WU Yong-hong, WU Hai-yan, XIE Jian-ping, LIU Xin-xing, QIU Guan-zhou. Treatment of backwater in bauxite flotation plant and optimization by using Box-Behnken design [J]. Transactions of Nonferrous Metals Society of China, 2019, 29(4): 821−830.

[8] DAI Min, XIA Ling, SONG Shao-xian, PENG Chang-sheng, RANGEL-MENDEZ J R, CRUZ-GAONA R. Electro-sorption of As(III) in aqueous solutions with activated carbon as the electrode [J]. Applied Surface Science, 2018, 434: 816−821.

[9] CHAN B K C, BOUZALAKOS S, DUDENEY A W L. Integrated waste and water management in mining and metallurgical industries [J]. Transactions of Nonferrous Metals Society of China, 2008, 18(6): 1497−1505.

[10] RAJENDRAN R M, GARG S, BAJPAI S. Economic feasibility of arsenic removal using nanofiltration membrane: A mini review [J]. Chemical Papers, 2021, 75(9): 4431−4444.

[11] FU Yun-feng, XIAO Qing-gui, GAO Yi-ying, NING Peng-ge, XU Hong-bin, ZHANG Yi. Direct extraction of Mo (VI) from acidic leach solution of molybdenite ore by ion exchange resin: Batch and column adsorption studies [J]. Transactions of Nonferrous Metals Society of China, 2018, 28(8): 1660−1669.

[12] YANG Jin-qin, CHAI Li-yuan, LI Qing-zhu, SHU Yu-de. Redox behavior and chemical species of arsenic in acidic aqueous system [J]. Transactions of Nonferrous Metals Society of China, 2017, 27(9): 2063−2072.

[13] LIANG Li-ping, XI Fen-fen, TAN Wei-shou, MENG Xu, HU Bao-wei, WANG Xiang-ke. Review of organic and inorganic pollutants removal by biochar and biochar-based composites [J]. Biochar, 2021, 3(3): 255−281.

[14] CUI Jie, DU Ya-guang, XIAO Hong-xia, YI Qiu-shi, DU Dong-yun. A new process of continuous three-stage co-precipitation of arsenic with ferrous iron and lime [J]. Hydrometallurgy, 2014, 146: 169−174.

[15] HUA Jin-ming. Adsorption of low-concentration arsenic from water by co-modified bentonite with manganese oxides and poly (dimethyldiallylammonium chloride) [J]. Journal of Environmental Chemical Engineering, 2018, 6(1): 156−168.

[16] MOHAN D, PITTMAN C U Jr. Arsenic removal from water/ wastewater using adsorbents—A critical review [J]. Journal of Hazardous Materials, 2007, 142(1/2): 1−53.

[17] LAI Li, XIE Qiang, CHI Li-na, GU Wei, WU De-yi. Adsorption of phosphate from water by easily separable Fe_3O_4@SiO_2 core/shell magnetic nanoparticles functionalized with hydrous lanthanum oxide [J]. Journal of Colloid and Interface Science, 2016, 465: 76−82.

[18] WANG Jing. Preparation and evaluation of zirconium-based materials for fluoride and arsenic removal from water [D]. Hefei: University of Science and Technology of China, 2014. (in Chinese)

[19] MANDAL S, MAHAPATRA S S, SAHU M K, PATEL R K. Artificial neural network modelling of As(III) removal from water by novel hybrid material [J]. Process Safety and Environmental Protection, 2015, 93: 249−264.

[20] SHI Qian-tao, YAN Li, CHAN Ting-shan, JING Chuan-yong. Arsenic adsorption on lanthanum-impregnated activated alumina: Spectroscopic and DFT study [J]. ACS Applied Materials & Interfaces, 2015, 7(48): 26735−26741.

[21] DENG Shu-bo, LI Zhi-jian, HUANG Jun, YU Gang. Preparation, characterization and application of a Ce−Ti oxide adsorbent for enhanced removal of arsenate from water [J]. Journal of Hazardous Materials, 2010, 179(1/2/3): 1014−1021.

[22] ZHAO Xiao-li, LIU Shuang-liu, WANG Pei-fang, TANG Zhi, NIU Hong-yun, CAI Ya-qi, WU Feng-chang, WANG Hao, MENG Wei, GIESY J P. Surfactant-modified flowerlike layered double hydroxide-coated magnetic nanoparticles for preconcentration of phthalate esters from environmental water samples [J]. Journal of Chromatography A, 2015, 1414: 22−30.

[23] ZHAO Lei, GE Xiao-qian, YAN Gui-hua, WANG Xiao, HU Peng-fei, SHI Li-yi, WOLFBEIS O S, ZHANG Hong-jie, SUN Li-ning. Double-mesoporous core−shell nanosystems

based on platinum nanoparticles functionalized with lanthanide complexes for in vivo magnetic resonance imaging and photothermal therapy [J]. Nanoscale, 2017, 9(41): 16012−16023.

[24] CHEN Yu, CHEN Hang-rong, GUO Li-min, HE Qian-jun, CHEN Feng, ZHOU Jian, FENG Jing-wei, SHI Jian-lin. Hollow/rattle-type mesoporous nanostructures by a structural difference-based selective etching strategy [J]. ACS Nano, 2010, 4(1): 529−539.

[25] GOLDBERG S, JOHNSTON C T. Mechanisms of arsenic adsorption on amorphous oxides evaluated using macroscopic measurements, vibrational spectroscopy, and surface complexation modeling [J]. Journal of Colloid and Interface Science, 2001, 234(1): 204−216.

[26] CARIONI V M O, MCELROY J A, GUTHRIE J M, NGWENYAMA R A, BROCKRMAN J D. Fast and reliable method for As speciation in urine samples containing low levels of As by LC-ICP-MS: Focus on epidemiological studies [J]. Talanta, 2017, 165: 76−83.

[27] YANG Yu, ZHANG Cheng-yu, YANG Li-ming, CHEN J P. Cerium oxide modified activated carbon as an efficient and effective adsorbent for rapid uptake of arsenate and arsenite: Material development and study of performance and mechanisms [J]. Chemical Engineering Journal, 2017, 315: 630−638.

[28] NAKAMOTO K, KOBAYASHI T. Arsenate and arsenite adsorbents composed of nano-sized cerium oxide deposited on activated alumina [J]. Separation Science and Technology, 2019, 54(4): 523−534.

[29] LIU Xue-wei, ZHANG Guo-gang, LIN Li-na, KHAN Z H, QIU Wei-wen, SONG Zheng-guo. Synthesis and characterization of novel Fe−Mn−Ce ternary oxide-biochar composites as highly efficient adsorbents for As(III) removal from aqueous solutions [J]. Materials, 2018, 11(12): 2445.

[30] ZHANG Yan-yang, SHE Xin-wei, GAO Xiang, SHAN Chao, PAN Bing-cai. Unexpected favorable role of Ca^{2+} in phosphate removal by using nanosized ferric oxides confined in porous polystyrene beads [J]. Environmental Science & Technology, 2019, 53(1): 365−372.

[31] ZHU Jun, PIGNA M, COZZOLINO V, CAPORALE A G, VIOLANTE A. Higher sorption of arsenate versus arsenite on amorphous Al-oxide, effect of ligands [J]. Environmental Chemistry Letters, 2013, 11(3): 289−294.

[32] CHANG Qi-gang, LIN Wei, YING Wei-chi. Preparation of iron-impregnated granular activated carbon for arsenic removal from drinking water [J]. Journal of Hazardous Materials, 2010, 184(1/2/3): 515−522.

[33] XU Zhi-gao, WU Yan-ke, ZHANG Jian-dong, ZHANG Li, WANG Li-jun. Equilibrium and kinetic data of adsorption and separation for zirconium and hafnium onto MIBK extraction resin [J]. Transactions of Nonferrous Metals Society of China, 2010, 20(8): 1527−1533.

[34] SHU Zeng-niang, XIONG Chun-hua, WANG Xu. Adsorption behavior and mechanism of amino methylene phosphonic acid resin for Ag (I) [J]. Transactions of Nonferrous Metals Society of China, 2006, 16(3): 700−704.

[35] WANG Wen-qing, LI Ming-yu, ZENG Qing-xuan. Thermodynamics of Cr (VI) adsorption on strong alkaline anion exchange fiber [J]. Transactions of Nonferrous Metals Society of China, 2012, 22(11): 2831−2839.

[36] MASUE Y, LOEPPERT R H, KRAMER T A. Arsenate and arsenite adsorption and desorption behavior on coprecipitated aluminum: Iron hydroxides [J]. Environmental Science & Technology, 2007, 41(3): 837−842.

[37] RAHDAR S, TAGHAVI M, KHAKSEFIDI R, AHMADI S. Adsorption of arsenic (V) from aqueous solution using modified saxaul ash: Isotherm and thermodynamic study [J]. Applied Water Science, 2019, 9(4): 1−9.

[38] YE Zhi-xin. Experimental study of the adsorption of arsenic (III) to the amino-modified carbon nanotubes/polyaniline [D]. Guangzhou: Jinan University, 2019. (in Chinese)

[39] LUO Su-shuang, YANG Chun-ping, HE Hui-jun, LONG Zhi-yong, CHENG yan. Synthesis of TiO_2/chitosan/graphene oxide adsorbent beads for adsorption of As(III) [J]. Chinese Journal of Environmental Engineering, 2016, 10(9): 4873−4878. (in Chinese)

[40] NASIR A M, GOH P S, ISMAIL A F. Novel synergistic hydrous iron-nickel-manganese (HINM) trimetal oxide for hazardous arsenite removal [J]. Chemosphere, 2018, 200: 504−512.

[41] MORENO-PIRAJÁN J C, GIRALDO L. Activated carbon from bamboo waste modified with iron and its application in the study of the adsorption of arsenite and arsenate [J]. Central European Journal of Chemistry, 2013, 11(2): 160−170.

[42] TÜRK T, ALP İ, DEVECI H. Adsorptive removal of arsenite from water using nanomagnetite [J]. Desalination and Water Treatment, 2010, 24(1/2/3): 302−307.

[43] ZENG Le. Arsenic adsorption from aqueous solutions on an Fe(III)−Si binary oxide adsorbent [J]. Water Quality Research Journal of Canada, 2004, 39(3): 267−275.

[44] BAGHERIFAM S, KOMARNENI S, LAKZIAN A, FOTOVAT A, KHORASANI R, HUANG Wen-yan, MA Jian-feng, WANG Yu-jue. Evaluation of Zn−Al−SO_4 layered double hydroxide for the removal of arsenite and arsenate from a simulated soil solution: Isotherms and kinetics [J]. Applied Clay Science, 2014, 95: 119−125.

[45] GHOSH D, BHATTACHARYYA K G. Adsorption of methylene blue on kaolinite [J]. Applied Clay Science, 2002, 20(6): 295−300.

[46] JAIN R, SHRIVASTAVA M. Adsorptive studies of hazardous dye Tropaeoline 000 from an aqueous phase on to coconut-husk [J]. Journal of Hazardous Materials, 2008, 158(2/3): 549−556.

[47] XU Wei-hong, WANG Jing, WANG Lei, SHENG Guo-ping, LIU Jin-huai, YU Han-qing, HUANG Xing-jiu. Enhanced arsenic removal from water by hierarchically porous CeO_2−ZrO_2 nanospheres: Role of surface- and structure-dependent properties [J]. Journal of Hazardous Materials, 2013, 260: 498−507.

[48] WEN Zhi-pan, ZHANG Ya-lei, GUO Sheng, CHEN Rong. Facile template-free fabrication of iron manganese bimetal oxides nanospheres with excellent capability for heavy metals removal [J]. Journal of Colloid and Interface Science, 2017, 486: 211−218.

[49] LUO Xu-biao, WANG Cheng-cheng, WANG Li-chuan, DENG Fang, LUO Sheng-lian, TU Xin-man, AU C T. Nanocomposites of graphene oxide-hydrated zirconium

oxide for simultaneous removal of As(III) and As(V) from water [J]. Chemical Engineering Journal, 2013, 220: 98−106.
[50] SIDDIQUI S I, CHAUDHRY S A. A review on graphene oxide and its composites preparation and their use for the removal of As^{3+} and As^{5+} from water under the effect of various parameters: Application of isotherm, kinetic and thermodynamics [J]. Process Safety and Environmental Protection, 2018, 119: 138−163.

磁性核壳结构 Ce 掺杂氧化锆的制备及其 As(III)吸附性能

杜明翰[1]，杨 虹[1]，付 翁[2]，胡燕玲[1]，陶 欢[1]，
范家喜[3]，刘 营[1]，陈宇凡[1]，迪莉娜尔[1]，刘晓箐[1]

1. 中国矿业大学 江苏省资源环境信息工程重点实验室，徐州 221116；
2. School of Chemical Engineering, The University of Queensland, St Lucia, Queensland 4072, Australia；
3. 南京汐泽水利技术有限公司，南京 210000

摘 要：采用溶剂热法和溶胶–凝胶法制备磁性介孔 As(III)吸附剂 Fe_3O_4@SiO_2@Ce-ZrO_2。该核壳结构材料具有高比表面积(168.2 m^2/g)和快速磁分离性能(5.37 $A·m^2/kg$)。与 Fe_3O_4@SiO_2@ZrO_2 相比，Ce 掺杂样品的 As(III)平衡吸附量提高 12%−23%(pH 3−11)，这主要归因于双金属 M—O—As 配合物的形成。共存的 SO_4^{2-} 和 PO_4^{3-} 会削弱 As(III)的吸附，Ca^{2+}对除 As(III)有积极作用，而 Cl^-和 NO_3^- 的影响很小。在初始 As(III)浓度 5 mg/L、313 K 和 pH 中性条件下，As(III)最大吸附容量可达 24.52 mg/g。准二级模型对 As(III)吸附动力学数据的拟合效果良好。此外，吸附剂再生性好。研究结果表明，Fe_3O_4@SiO_2@Ce-ZrO_2 适于含 As(III)废水的深度处理，具有良好的应用前景。

关键词：核壳结构；磁性；铈掺杂；氧化锆；As(III)吸附

(Edited by Xiang-qun LI)